Mechanical Systems and Signal Processing 237 (2025) 112890

Contents lists available at ScienceDirect

Mechanical Systems and Signal Processing

journal homepage: www.elsevier.com/locate/ymssp

Full length article

Simultaneous viscoelastic characterization of soft tissues based on shear wave ultrasound dispersion and multi-scale wavelet cross-correlation analysis

Shihao Cui [a,b,c], Guy Cloutier [b,d,e], Marie-Hélène Roy Cardinal [d], Houman Savoji [b,c,g,*], Pooneh Maghoul [a,f,**]

[a] Sustainable Infrastructure and Geoengineering Lab (SIGLab), Department of Civil, Geological and Mining Engineering, Polytechnique Montréal, Montreal, Quebec, Canada
[b] Institute of Biomedical Engineering, Department of Pharmacology and Physiology, Faculty of Medicine, University of Montréal, Montreal, Quebec, Canada
[c] CHU Sainte Justine Research Center, Montreal, Canada
[d] Laboratory of Biorheology and Medical Ultrasonics, University of Montréal Hospital Research Center (CRCHUM), Montreal, Quebec, Canada
[e] Department of Radiology, Radio-oncology, and Nuclear Medicine, University of Montréal, Montreal, Quebec, Canada
[f] United Nations University Institute for Water, Environment and Health (UNU-INWEH), Richmond Hill, Ontario, Canada
[g] Department of Mechanical Engineering, Institute of Biomedical Engineering, Polytechnique Montreal, Montreal, Quebec, Canada

ARTICLE INFO

Communicated by M. Rebillat

Keywords:
Soft tissue
Viscoelasticity
Ultrasound shear waves
Wavelet cross-correlation analysis
Simulated annealing

ABSTRACT

Ultrasound shear waves offer a non-destructive testing approach to assess the biomechanical properties of biological soft tissues. This paper presents a method based on the dispersion relations of ultrasound shear waves to inversely derive the viscoelastic properties of soft tissues. In the proposed method, dispersion relations are extracted from shear wave signals based on the multi-scale wavelet correlation analysis. Here, the continuous wavelet transform is employed to convert shear wave signals into various frequencies. The cross-correlation method is utilized to obtain the phase velocity of the shear waves. This approach offers advantages, including multiscale analysis capability, high-resolution time–frequency representation, flexible parameter selection, and continuous time–frequency scaling. Subsequently, an inversion process utilizing the simulated annealing algorithm is designed to characterize the properties of soft tissues. The effectiveness and accuracy of the proposed approach have been verified numerically and experimentally.

1. Introduction

The mechanical properties of biological soft tissues, including stress–strain relationships, stiffness, elasticity, and viscosity, can be an indicator of the physiological and pathological states of biological tissues. The foundation of pathology lies in changes to the molecular structure or composition of biological tissues. For instance, diseases such as sclerotic breast cancer [1], atherosclerosis [2], and prostate cancer [3] often exhibit an increase in tissue stiffness compared to pre-disease conditions, especially in the early stages of disease development. Additionally, changes in the viscosity of soft tissues may indicate the presence of an inflammatory process,

* Corresponding author at: Department of Mechanical Engineering, Institute of Biomedical Engineering, Polytechnique Montreal, Montreal, Quebec, Canada.
** Corresponding author at: Sustainable Infrastructure and Geoengineering Lab (SIGLab), Department of Civil, Geological and Mining Engineering, Polytechnique Montréal, Montreal, Quebec, Canada.
E-mail addresses: h.savoji@polymtl.ca (H. Savoji), pooneh.maghoul@polymtl.ca (P. Maghoul).

https://doi.org/10.1016/j.ymssp.2025.112890
Received 5 August 2024; Received in revised form 18 April 2025; Accepted 20 May 2025
Available online 19 June 2025

which can lead to fluid accumulation, increased cellular activity, or metabolic changes [4]. The characterization of viscoelastic properties is widely used in diagnosing conditions such as cancer [5], liver fibrosis [6], and cardiovascular diseases [7]. Furthermore, monitoring changes in the viscoelastic properties of tissues during treatment can be used to assess therapeutic outcomes [8]. In the design and fabrication of artificial tissues or biomaterials, such as during 3-dimensional (3D) printing, understanding their viscoelastic properties is crucial for mimicking the mechanical behavior of natural tissues [9].

To effectively and accurately monitor or measure the viscoelastic properties of soft tissues, a variety of methods have been proposed in the literature. Non-destructive testing (NDT), known for its non-invasive nature and convenience, has been widely utilized in this field [10,11]. Techniques such as indentation testing, magnetic resonance elastography (MRE), and ultrasound elastography are among the methods employed. Indentation testing quantifies the mechanical properties of materials by measuring the force applied by an indenter and recording the force–displacement curve. This curve, combined with specific models or empirical formulas, is used to calculate the material's mechanical parameters [12,13]. By analyzing the force–displacement curve, indentation testing typically measures the overall mechanical properties of a material but is unable to assess the distribution of internal properties. For materials with heterogeneity or anisotropy, this method may not accurately describe their complex internal structures. MRE is an advanced technique within the realm of magnetic resonance imaging (MRI). While MRI relies on electromagnetic waves to capture intricate images of the internal structures of biological materials, MRE takes this a step further by incorporating mechanical vibrations that create shear waves within the tissues [14]. These waves are subsequently tracked and measured utilizing MRI technology. Viscoelastic properties of the tissue are then assessed through analysis of MRI images of recorded waves. This method has played a significant role in areas such as liver fibrosis [15] and cardiac imaging [16]. However, this method is relatively costly and may require a significant amount of time to perform.

Ultrasound elastography offers low cost and high operability, leading to extensive application of this technology for measuring the viscoelastic properties of soft tissues. Traditional ultrasound techniques use static strain estimation methods [17]. This involves applying a static force to the soft tissue, causing it to deform. When ultrasound waves are used for detection, the echoes also change. By comparing ultrasound echoes before and after the application of a force, this method determines the displacement distribution under external force to estimate the tissue's deformation or Young's modulus using an inversion algorithm [18]. These methods utilize compression waves for displacement tracking and often involve manually applied pressure, or the natural pulsation of an organ. However, for the remote examination of internal organs and other deeper tissues, the applied pressure may not adequately propagate to the target depth. Another ultrasound elastography technique is based on shear waves. Transient elastography (TE) involves applying a push with a probe to the surface of the tissue to generate transient shear deformation that propagates into the tissue. The velocity of the shear wave near the source of excitation can be obtained by recording the ultrasound echo signals [19]. This method typically permits the estimation of the tissue's shear modulus or Young's modulus (usually considering Poisson's ratio of soft tissue close to 0.5) [20].

Shear wave elastography (SWE), a pivotal technique in the field of ultrasound elastography, has emerged as a mainstream technology in clinical elastographic imaging. It is distinguished by its high resolution, quantifiability, and extensive applicability across various clinical settings. Compared with TE, SWE can provide regional or global elasticity information, offering broader applicability and precise localization of pathological areas. TE typically yields a single elasticity value; its operation is relatively straightforward but lacks imaging capabilities. SWE can estimate the viscoelasticity of a medium using the frequency-dependent dispersion properties of shear wave speed in viscoelastic media [21,22]. Typically, this method relies on acoustic radiation force (ARF) to generate shear waves. Shear wave phase velocities are analyzed by measuring signals at certain space intervals. To accurately obtain dispersion relations, various methods have been proposed. For instance, the work [23] applied different frequencies of excitation to measure the corresponding shear wave speeds and obtain dispersion relations. The work [24] introduced a technique where multi-frequency external sources are employed to generate simultaneous multi-frequency reverberant shear wave fields for viscoelasticity analysis. The studies [25,26] adjust the distances between signal collection points to obtain dispersion relation. The research [27] developed a novel supersonic shear imaging technique for the in vivo quantitative mapping of liver viscoelasticity. The time-of-flight technique is utilized to recover shear wave velocities, enabling the acquisition of dispersion relations for the quantitative two-dimensional mapping of shear elasticity. The study [28] employed Doppler imaging technology to analyze the dispersion of shear wave velocity and attenuation, aiming to assess liver conditions such as steatosis.

Dispersion relations are typically extracted from spatiotemporal ultrasound data. Different methods have been proposed to extract dispersion relations. For example, phase gradient algorithms have been used to analyze the phase of shear waves at different frequencies at multiple lateral positions relative to the location of ARF application [29]. Methods using two-dimensional Fourier transform (2DFT) have also been applied to process spatiotemporal shear wave data and extract dispersion relations [30,31]. However, Fourier transform-based methods may be limited by noise, spatial, and temporal sampling. The work [32] proposed a method based on continuous wavelet transform (CWT), originally developed for extracting the dispersion relations of seismic waves, to analyze ultrasound shear waves. This approach requires the use of Green's functions to compute phase difference, where a parameter determined by phase data and wave propagation characteristics must be predefined through optimization fitting or prior knowledge. The parameter pre-determination may pose an inconvenience. Moreover, the study did not account for the multi-scale nature of CWT and did not utilize dispersion curves to inversely estimate the viscoelastic properties of soft tissues. CWT is a commonly used method in signal processing, and one of its primary objectives is to transform a time-domain signal into different frequencies or scales. CWT offers a flexible way to analyze signals by adjusting its resolution to the signal's frequency content, unlike the fixed resolution of Fourier transform (FT). This adaptability makes WT ideal for non-stationary signals with changing statistical properties over time, which FT cannot handle as effectively. WT's multi-scale analysis captures both local details and overall trends, and its localization in time and frequency allows for precise identification of signal features. It is also more noise-resistant, thanks

to its selective design to respond to signal characteristics [33]. Therefore, this paper proposes a method based on multiscale wavelet cross-correlation (WCC) analysis to enhance the stability and noise resistance of dispersion relation extraction. In the proposed method, the CWT is employed to convert spatiotemporal shear wave data into various frequencies. The cross-correlation method is subsequently utilized to determine time delays, thus obtaining the phase velocity of the shear waves. This approach offers several advantages, including multiscale analysis capability, high-resolution time–frequency representation, the elimination of the need for window functions and the selection of parameters for Green's function, and continuous time–frequency scaling.

As mentioned above, the extraction of dispersion relations may be used to characterize the viscoelastic properties of soft tissues by SWE. Several studies have been conducted to characterize viscoelasticity, with the main challenge lying in the frequency-dependent sensitivity of the parameters. For example, the study [34] obtained low-frequency dispersion relations (50 to 150 Hz) using MRI, which can further be used to analyze the shear modulus of soft tissues. However, this approach is highly susceptible to noise interference and requires high-quality data acquisition equipment, making it challenging to achieve accurate results in practice. The work [35,36] employed the least squares (LS) fitting method for parameter estimation. However, the inversion methods based on LS are prone to noise and disturbances during the dispersion extraction process, which may cause the results to depend heavily on local data characteristics, potentially leading to overfitting. The simulated annealing (SA) algorithm, due to its strong search capability, is better equipped to handle such noise or disturbances and to find more stable solutions. Therefore, in this study, an SA-based inversion algorithm is proposed to characterize the viscoelasticity of soft tissues. The proposed method is first validated through numerical analysis. In numerical analysis, the impact of wave signals with varying levels of noise on the proposed method for extracting dispersion relations has been studied, demonstrating the method's robust noise resistance. A filter based on discrete wavelet transform is established to handle heavy noise signals. The proposed method has been effectively applied to the inversion of viscoelastic properties in live ducks' livers with different fat contents, which validates the effectiveness and accuracy of the proposed dispersion relation extraction method and inversion process.

2. Methodology

The complete flowchart of the method proposed in this paper is shown in Fig. 1. The proposed method consists of the following steps: the first step is data collection (as explained in Section 2.1). The second step involves extracting the experimental dispersion relations based on WCC analysis (as explained in Section 2.3). The third step is the inverse estimation of soft tissue's viscoelastic properties based on the simulated annealing algorithm (SA) (as explained in Section 2.5). During the inversion process, the forward model is used to compute the theoretical dispersion relations (as explained in Section 2.4). Those steps are explained in the following sections.

2.1. Experimental setup and data acquisition

The experimental setup, as shown in Fig. 1(a), involves applying a given excitation to the external surface of the soft tissue, typically in the form of acoustic force pushes. Two ultrasound sensors are positioned at distances r_1 and r_2 from the point of excitation application, where $\Delta r = r_2 - r_1$. The collected displacement signals in the z direction (the axial dimension defined in the coordinate system in Fig. 1(a)) are denoted as S_1 and S_2, representing the induced shear waves.

2.2. Ultrasound shear waves

For homogeneous viscoelastic materials, Navier's equation governs the behavior of shear waves. This equation can be expressed as,

$$\mu \nabla^2 \mathbf{u} = \rho \frac{\partial^2 \mathbf{u}}{\partial t^2} \tag{1}$$

in which ρ is the density; $\mathbf{u}$ is the displacement vector; μ refers to the shear modulus and is a complex number. In this paper, the Kelvin–Voigt viscoelastic model is used to define the shear modulus μ, since it shows a better performance for soft tissue modeling [37], i.e., $\mu = \mu_1 + i\omega\mu_2$, and μ_1 is the shear elasticity and μ_2 refers to the viscosity; i is the imaginary unit ($i = \sqrt{-1}$); ω is the angular frequency. The problem is reformulated in a cylindrical coordinate system (r, θ, z). The displacement component in the z direction can be expressed as Chen et al. [38],

$$u(r) = \frac{De^{-k_I r}}{\sqrt{r}} e^{ik_R r}. \tag{2}$$

where D is a term that is independent of the variable r; the complex wavenumber $k = k_R + ik_I$, where k_R is the real part of k, and k_I is the imaginary part of k. k, k_R, and k_I are all functions of frequency. Therefore, the general solution of the shear wave is a function of frequency and can be analyzed at each frequency component.

Utilizing Euler's equation, expressed as $e^{ix} = \cos x + i \sin x$, where x is a variable, Eq. (2) can be expanded to $u(r) = \frac{De^{-k_I r}}{\sqrt{r}} \left[\cos(k_R r) + i \sin(k_R r)\right]$. It can be found that the phase of $u(r)$ can be calculated as $\arctan(\frac{\sin(k_R r)}{\cos(k_R r)}) = \arctan(\tan(k_R r)) = k_R r$. For two signals collected at positions r_1 and r_2, denoted by $u(r_1)$ and $u(r_2)$, the phase difference (ϕ_s) can be computed as $\phi_s = k_R \Delta r$, where $\Delta r = r_2 - r_1$. Given that $k_R = \omega / c_s$, we can deduce $c_s(f) = \frac{\Delta r}{\phi_s / \omega}$, where the term $\frac{\phi_s}{\omega}$ refers to the time lag of the signals $u(r_1)$ and $u(r_2)$ (that is, S_1 and S_2) at the frequency ω.

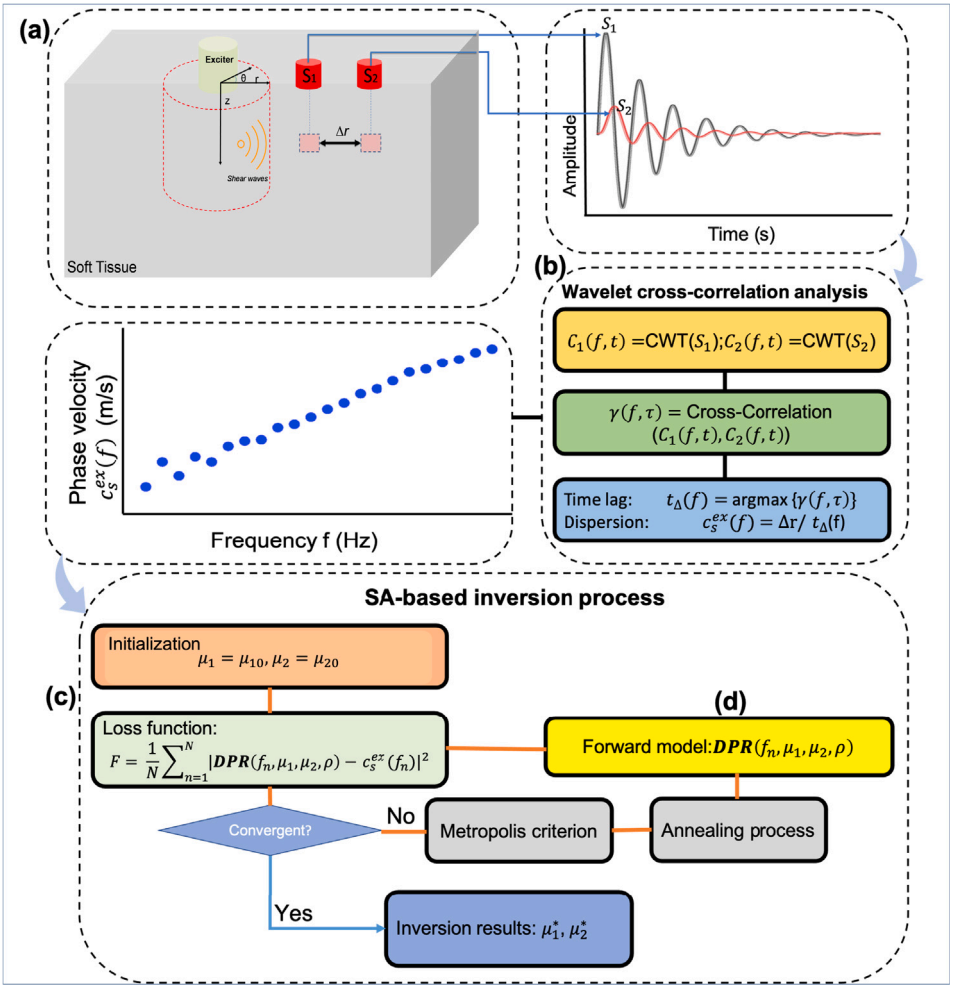

Fig. 1. The schematic diagram of the SA-based characterization using the wave cross-correlation analysis-extracted dispersion relation. (a). The setup for data acquisition: S_1 and S_2 are the two collected signals. (b). The experimental dispersion relation ($c_s^{ex}(f)$) extraction process using WCC analysis. (c). The SA-based inversion process for the soft tissue viscoelasticity characterization, where μ_1: shear modulus, μ_2: viscosity, ρ: density; μ_{10} and μ_{20} are the initialized values of μ_1 and μ_2, respectively; μ_1^* and μ_2^* are the inverted results of μ_1 and μ_2, respectively. (d). The forward model (**DPR**(.)).

2.3. Dispersion relation extraction based on the WCC analysis

In this work, we propose a method that utilizes wavelet transform (WT) and cross-correlation analysis to extract the dispersion relation of the phase velocity $c_s(f)$ at varying frequencies, based on the two signals S_1 and S_2. The CWT is applied to decompose the signals into different frequency components [39,40]. The CWT for a given signal, $x(t)$, can be expressed as,

$$C_{wt}(a,b) = \frac{1}{\sqrt{a}} \int_{-\infty}^{+\infty} x(t) \cdot \psi^* \left(\frac{t-b}{a} \right) dt, \tag{3}$$

where $\psi(.)$ is the wavelet basis function and $\psi^*(.)$ is its complex conjugate function; a is the scale parameter, responsible for the width of the wavelet basis function, while b is the translation parameter, responsible for the position of time of the wavelet basis function. The scale parameter a can be related to the frequency and in CWT, the frequency value f_a corresponding to the scale parameter a can be approximated as $f_a = \frac{F_c F_s}{a}$, where F_c is the center frequency of the selected wavelet basis function($\psi(.)$) and F_s is the sampling frequency of the input signal. In this study, the complex Morlet wavelet is chosen as the basis function [41]. This selection is attributed to its excellent capability in capturing local features and frequency characteristics of signals, which is crucial for effective time–frequency analysis [42].

The procedure of the proposed method (WCC) for the dispersion relation of phase wave velocity $c_s(f)$ is elaborated as follows:

1. For the signals S_1 and S_2 collected at positions r_1 and r_2 respectively, the result of the CWT, C_{wt}, is computed using Eq. (3). The outcomes for these signals are denoted as $C_1(f,t)$ and $C_2(f,t)$, corresponding to each signal. In the investigated area,

pairs at different positions can be selected for dispersion extraction to increase the robustness. The frequency variable f is within the range of Ω, where Ω is a vector that starts at $\frac{F_{max}}{N_s}$, increments by $\frac{F_{max}}{N_s}$, and goes up to $F_{\max}$. Here, $F_{\max}$ represents the maximum frequency for time–frequency analysis, and N_s is used to denote the frequency resolution for time–frequency analysis. A larger value of N_s implies more frequency components, while a smaller value of N_s implies fewer frequency components. The parameter N_s is instrumental in regulating the number of sample points on the dispersion curve. To increase the density of sample points, N_s can be reduced, which enhances the stability of the dispersion curve results. Moreover, certain scale parameters of the WT may resonate with noise elements within the signal, thereby influencing the accuracy of the results. To counteract this, one can iteratively adjust the ranges of Ω and N_s to mitigate the effects of noise.

2. At a specific frequency f, the cross-correlation, γ, of $C_1(f,t)$ and $C_2(f,t)$ can be obtained by Cheng and Pellettiere [43],

$$\gamma(f,\tau) = \int_{-\infty}^{+\infty} \bar{C}_2(f,t+\tau)\cdot \bar{C}_1(f,t)dt, \tag{4}$$

Here, $\bar{C}_1(f,t)$ and $\bar{C}_2(f,t)$ are the normalized versions of $C_1(f,t)$ and $C_2(f,t)$, respectively, scaled to the [0,1] range. This normalization aims to enhance the stability of the correlation calculation. τ represents the time lag between the signal components $\bar{C}_1(f,t)$ and $\bar{C}_2(f,t)$ at the frequency f. $\gamma(f,\tau)$ indicates the correlation at different time delays (τ) between $\bar{C}_1(f,t)$ and $\bar{C}_2(f,t)$. When the collected signals are severely noisy, their cross-correlation might exhibit some singularities, which could affect the identification of time lags. To enhance the stability of time lag identification, a 5-layer wavelet threshold filter has been designed to process the cross-correlation when the collected signals are heavily affected by noise. This wavelet threshold filter is described in detail in Appendix B.

3. At different frequencies, the results of the CWT exhibit pseudoperiodicity. Therefore, for the components $\bar{C}_1(f,t)$ and $\bar{C}_2(f,t)$ at a specific frequency f, the time lag (t_Δ) between these two pseudoperiodic functions can be determined by the time component (τ) corresponding to the maximum correlation. This is because when $\bar{C}_2(f,t)$ is shifted forward by t_Δ seconds on the time axis, the similarity between $\bar{C}_1(f,t)$ and $\bar{C}_2(f,t)$ reaches its peak. Therefore, there is,

$$t_\Delta(f) = \arg\max_{\tau}\{\gamma(f,\tau)\}, \tag{5}$$

4. Since $t_\Delta(f)$ represents the phase difference in the time dimension between the components $\bar{C}_1(f,t)$ and $\bar{C}_2(f,t)$ at different frequencies, the phase velocity at the frequency f, denoted as $c_s(f)$, can be calculated by

$$c_s(f) = \frac{\Delta r}{t_\Delta(f)}, \tag{6}$$

where the wavenumber-frequency dispersion relation based on WCC can be expressed as $k_R(f) = \frac{2\pi f * t_\Delta(f)}{\Delta r}$. Steps (2) through (4) outline the process of calculating the phase velocity at a specific frequency f. By repeating this process for different frequencies within the set $f \in \Omega$, the dispersion relation for these frequencies can be determined.

The above procedures of WCC analysis for dispersion relation extraction can be summarized in Algorithm 1.

Algorithm 1 The procedure of WCC analysis.

Initialization: $i = 1$, F_{max}, N_s, Ω, $C_1(\Omega,t)$, $C_2(\Omega,t)$,
while $i \le N_s$ **do**
  $f \leftarrow \Omega[i]$
  $\gamma(f,\tau) \leftarrow \int_{-\infty}^{+\infty} \bar{C}_2(f,t+\tau)\cdot \bar{C}_1(f,t)dt$
  $t_\Delta(f) \leftarrow \arg\max_{\tau}\{\gamma(f,\tau)\}$
  $c_s(f) \leftarrow \Delta r / t_\Delta(f)$
  $i++$
end while
Output the phase velocity $c_s(\Omega)$ of the input frequency vector Ω

2.4. Theoretical dispersion relation

The complex wavenumber k can be computed using the formula $k = \frac{\omega}{c}$, where the wave velocity c is a complex number. This velocity is given by $c = \sqrt{\frac{\mu}{\rho}}$; therefore, the complex wavenumber k can be calculated as:

$$k = \frac{\omega\sqrt{\rho}}{\sqrt{\mu_1^2+\mu_2^2\omega^2}}\sqrt{\mu_1 - i\omega\mu_2}, \tag{7}$$

The term $\sqrt{\mu_1 - i\omega\mu_2}$ can be calculated as $\sqrt{\mu_1 - i\omega\mu_2} = \sqrt{A}(\cos\frac{\hat{\theta}}{2} + i\sin\frac{\hat{\theta}}{2})$, where $A = \sqrt{\mu_1^2+\omega^2\mu_2^2}$ and $\hat{\theta} = \arccos\frac{\mu_1}{A}$.

The wavenumber-frequency dispersion relation can be obtained as, $k_R = \frac{\omega\sqrt{\rho}}{A}\sqrt{\frac{A+\mu_1}{2}}$. Here, the phase velocity ($c_s(f)$) of the shear waves can be defined as $c_s(f) = \frac{\omega}{k_R}$, that is,

$$c_s(f) = A\sqrt{\frac{2}{\rho(A+\mu_1)}}, \tag{8}$$

Here, the forward model, denoted by $\mathbf{DPR}(f, \mu_1, \mu_2, \rho)$, is defined to show the relation of the phase velocity, $c_s(f)$, at different frequencies according to Eq. (8).

2.5. Inversion based on SA

This paper proposes a method for characterizing the viscoelastic properties of soft tissues based on the SA algorithm. Its advantage lies in its insensitivity to initial values, effectively avoiding entrapment in local optima. The core ideas of SA include the annealing process and the Metropolis criterion [44]. For an annealing process implementation, we set an initial temperature, i.e., the maximum temperature $T_{\max}$, and a minimum temperature for annealing, $T_{\min}$. In each iteration $iter$, the temperature is updated as $T = \frac{T_{\text{old}}}{\log(1+iter)}$, where T_{old} is the temperature from the previous iteration. When the temperature decreases to a certain value T, a certain number of searches are conducted to update the solution. The new solution x_{new} is used to update the old one x_{old}. To ensure the convergence of the algorithm, at temperature T, the maximum number of updates for the new solution, $K_{\max}$, is set. Specifically, define $\Delta F = F(x_{\text{new}}) - F(x_{\text{old}})$, where $F(.)$ is the loss function. The Metropolis criterion states that when $\Delta F < 0$, there exists $e^{-\frac{\Delta F}{T}} > r_d$ where r_d is a random number in the range $[0, 1]$, the solution is updated with the new one.

According to the analytical dispersion relation, denoted by $\mathbf{DPR}(f_n, \mu_1, \mu_2, \rho)$, and utilizing the forward model in Eq. (8) along with the dispersion relation extracted by the proposed WCC analysis method in Algorithm 1, denoted by $c_s^{ex}(f_n)$ where f_n is the n^{th} frequency in the extracted dispersion relation, the loss function is defined as follows:

$$F = \frac{1}{N}\sum_{n=1}^{N}\left|\mathbf{DPR}(f_n, \mu_1, \mu_2, \rho) - c_s^{ex}(f_n)\right|, \tag{9}$$

where N is the total number of frequencies in the extracted dispersion relation. Based on this loss function in Eq. (9), the SA-based inversion process is described as follows:

Algorithm 2 The SA-based soft tissue viscoelasticity inversion.

Initialization: $\mu_1 = \mu_{10}$, $\mu_2 = \mu_{20}$, $iter = 1$, $T = T_{max}$, T_{min}, K_{max}, $iter_{max}$
while $iter \le iter_{max}$ **and** $T \ge T_{min}$ **do**
  $K = 1$
  while $K \le K_{max}$ **do**
    $x_{old} \leftarrow \{\mu_1, \mu_2\}$
    $x_{new} \leftarrow x_{old}$
    $\Delta F = F(x_{new}) - F(x_{old})$
    if $\Delta F \le 0$ **or** $[\Delta F > 0$ **and** $e^{(-\frac{\Delta F}{T})} > rand(0,1)]$ **then**
      $x_{new} = x_{old}$
    end if
    $K++$
  end while
  $T = \frac{T}{\log(1+iter)}$
  $iter++$
end while
Output the inversion result: μ_1^*, μ_2^*

3. Verification in silico

3.1. Data acquisition

To validate the reliability and accuracy of the method proposed in this paper, a numerical analysis is initially conducted. The data for this analysis is generated using the finite element method (FEM) model (the configuration is given in Appendix A). The material properties of the viscoelastic medium under study, along with the distances between the two sensor locations, are summarized in Table 1. Two cases of the soft tissues are analyzed, and specifically, in Case 1, the shear modulus and viscosity of the material are modeled to replicate the renal cortex of a swine kidney, as examined in the work [45]. The data simulation methods for these 2 cases are identical.

In this simulation, a sampling frequency of 10^5 Hz is configured, and the sampling time is 0.03 s. Therefore, at each receiver position, a time series with 3000 points can be obtained. Fig. 2(a) displays the waveform of the two collected signals, S_1 and S_2, respectively.

3.2. Dispersion relation extraction using WCC analysis

When the two signals S_1 and S_2 are obtained, following the procedure given in Algorithm 1, the dispersion relation can be extracted based on the proposed WCC analysis. In this section, the signal collected from Case 1 is used for illustration.

Table 1
The physical properties and the distance of the two receivers.

Parameter (unit)	Case 1	Case 2
Shear modulus μ_1 (Pa)	2300	7500
Viscosity μ_2 (Pa s)	2.2	7.2
Density ρ (kg/m^3)	1000	1000
Poisson's ratio ν	0.495	0.495
Receiver spacing Δr (mm)	2	2

The analysis begins by computing the CWT coefficients for S_1 and S_2, as prescribed by Eq. (3). The outcomes of the CWT, labeled as $C_1(f,t)$ for S_1 and $C_2(f,t)$ for S_2, are illustrated in Figs. 2(c) and (d) respectively. Typically, the dispersion characteristics of soft tissues are examined within a frequency range up to 500 Hz, yet the precise range should be adapted based on empirical data available [26,29,45]. For the numerical analysis in this research, the frequency spectrum is confined to [50,500] Hz. The highest frequency band considered, $F_{\max}$, is fixed at 500 Hz due to the primary observation of dispersive phenomena within this band [45]. First, the choice of $N_s = 24$ serves as a representative parameter value for method validation and performance evaluation. Then, by incrementally increasing N_s, we illustrate the effectiveness and adaptability of the WCC method in terms of frequency-domain resolution. In practical applications, N_s can be adjusted to balance the desired resolution and computational efficiency.

Fig. 2(b) gives the component of the CWT coefficient when $f = 416.67$ Hz, where the component of the CWT result has been normalized to [0,1], that is $\bar{C}_1(f,t)$ and $\bar{C}_2(f,t)$. In Fig. 2(b), it can be observed that the frequency components $\bar{C}_1(f,t)$ and $\bar{C}_2(f,t)$ are pseudo-periodic functions and their time lag is denoted as t_Δ. t_Δ here can be obtained by performing cross-correlation on the frequency components $\bar{C}_1(f,t)$ and $\bar{C}_2(f,t)$. The results of the cross-correlation analysis are presented in Fig. 3. At this frequency, the specific calculation process for t_Δ and the phase wave speed is as follows: The cross-correlation $\gamma(f,\tau)$ between these two components can be calculated at different times τ using Eq. (4). The time delay t_Δ is identified at the point where $\gamma(f,\tau)$ reaches its maximum, denoted by $Max\{\gamma(f,\tau)\}$. Here, t_Δ is identified as 6.1×10^{-4} s. Consequently, when $f = 416.67$ Hz, the phase velocity of the wave is calculated to be 3.28 m/s. By iterating the procedure demonstrated in Fig. 3, at the frequencies indicated in Fig. 2(c)(d), we can compute the phase velocity $c_s(f)$ at each frequency.

Fig. 4 displays the dispersion curves for three N_s values corresponding to parts (a), (b), and (c) of the figure. Fig. 4(a) illustrates the dispersion curves derived from the simulated signals S_1 and S_2 using the proposed WCC method, and compares them with the theoretical dispersion curves obtained from the forward model. The key observations from this comparison are: (1) The proposed method successfully extracts the dispersion relations from shear wave vibration signals with high accuracy. However, an anomaly is noted at extremely low frequencies, likely caused by wavelet transform distortions at these frequencies. Potential reasons include insufficient sampling frequency for the low-frequency components, leading to a violation of the Nyquist theorem, and signal edge effects that prevent a complete wavelet cycle at the signal's start and end. Despite this, the outlier is distinguishable and removable, thus not impeding the overall dispersion relation extraction. For frequencies above 50 Hz, the average precision (AP), as defined in Eq. (10), is found to be 98.13%, compared to the theoretical dispersion relation.

$$AP = \frac{1}{N_d}\sum_{i=1}^{N_d}\frac{|Y_i - \hat{Y}_i|}{Y_i}, \tag{10}$$

where $\hat{Y}_i$ is the ith extracted dispersion relation point and Y_i is the corresponding theoretical value. N_d is the total number of the extracted dispersion relation points.

Fig. 4(a) demonstrates the results for $N_s = 24$, whereas Fig. 4(b) shows the case for $N_s = 36$. Fig. 4(c) for $N_s = 45$ further illustrates the increased sample points. An increase in N_s leads to a higher number of sample points on the dispersion curve, enhancing its stability. The AP between the extracted dispersion relations and the theoretical models for N_s of 24, 36, and 45 can demonstrate the method's accuracy and stability.

Fig. 5 presents the dispersion relations extracted using the WCC method for Cases 1 and 2 ($N_s = 24$), along with their corresponding analytical dispersion relations. The comparison shows that the performance of the proposed WCC method in extracting dispersion relations is commendable. The dispersion extraction based on 2DFT is also compared in the figure.

3.3. Noise resistance analysis

To test the stability and robustness of the proposed method against noise, this study firstly conducts the noise resistance analysis by adding white Gaussian noise (WGN) into the generated displacement waveforms at different levels. The noise level is controlled by setting various signal-to-noise ratios (SNR). Figs. 6 and 7 show the results of dispersion extraction at SNR levels of 40 dB and 20 dB, respectively. Signals for the analysis in this section are from Case 1.

Fig. 6 presents the dispersion extraction result at an SNR of 40 dB. Fig. 6(a) shows the signal with noise; Fig. 6(b) displays the normalized CWT coefficients at a frequency of 277.78 Hz, where the noise is quite noticeable; Fig. 6(c) shows the cross-correlation of the two components from Fig. 6(b), indicating that the cross-correlation remains stable even in the presence of noise. Fig. 6(d) illustrates the results of the proposed dispersion extraction method at an SNR of 40 dB, demonstrating its stability and high accuracy.

Fig. 7 presents the dispersion extraction result at an SNR of 20 dB. Fig. 7(a) shows the noisy signal; Fig. 7(b) displays the normalized CWT coefficients at a frequency of 375 Hz, where the noise is very severe; Fig. 7(c) shows the cross-correlation range

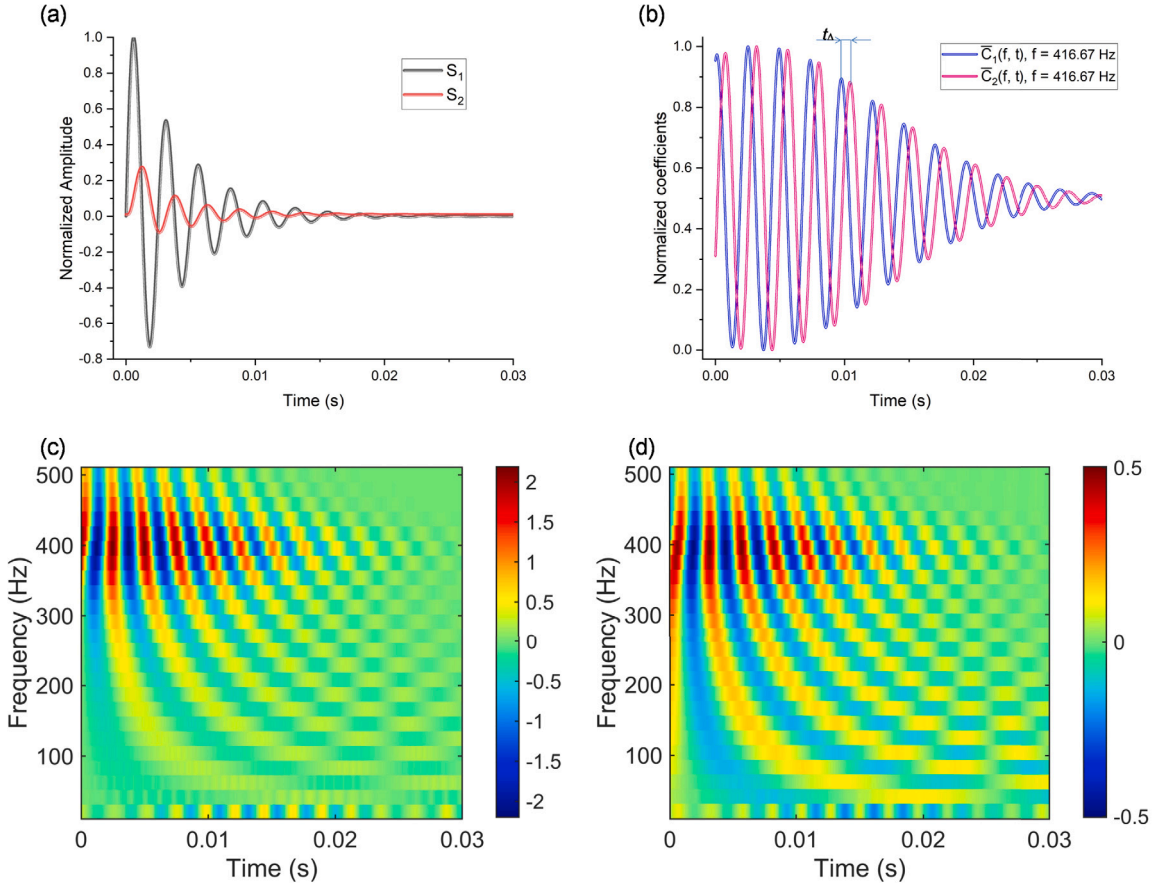

Fig. 2. The results of the CWT of the two given signals S_1 and S_2: (a) The two collected signals S_1 and S_2; (b) The normalized components of the CWT coefficients $C_1(f,t)$ and $C_2(f,t)$ at the frequency $f = 416.67$ Hz; (c) The CWT coefficient of Signal S_1, $C_1(f,t)$; (d) The CWT coefficient of Signal S_2, $C_2(f,t)$.

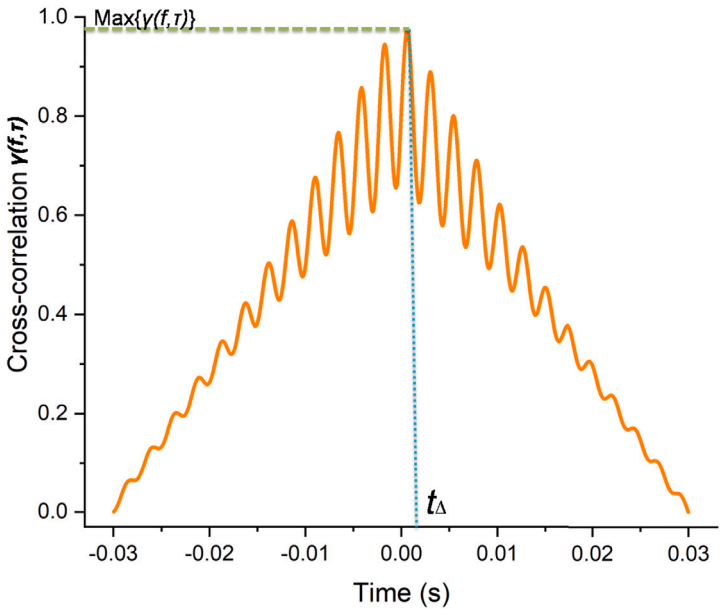

Fig. 3. The cross-correlation of $\bar{C}_1(f,t)$ and $\bar{C}_2(f,t)$ when $f = 416.67$ Hz.

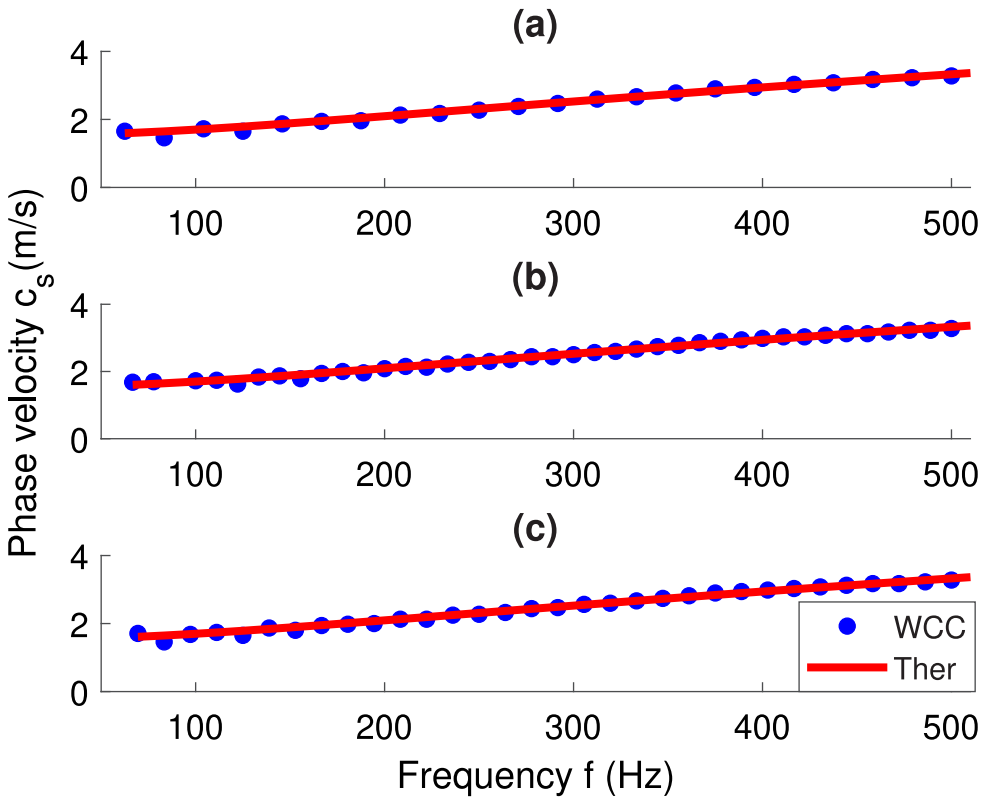

Fig. 4. Comparison of the extracted dispersion relation curves obtained through the proposed WCC analysis with those derived from the theoretical forward model; **Ther**: Theoretical model. (a). $N_s = 24$; (b). $N_s = 36$ (b). $N_s = 45$.

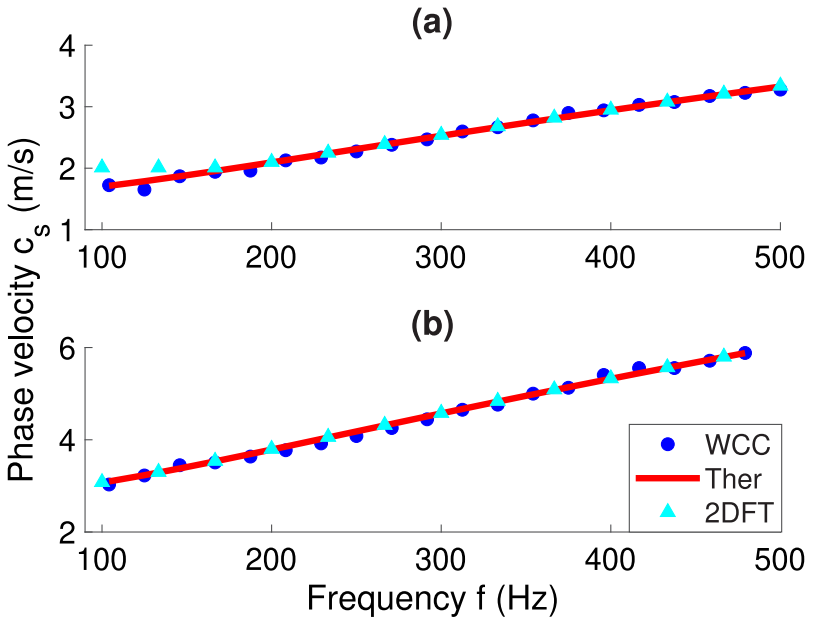

Fig. 5. The extracted dispersion relation curves for Cases 1 and 2; **Ther**: Theoretical model. (a). Case 1; (b). Case 2.

near the maximum of the cross-correlation of the two components from Fig. 7(b), revealing potential singularities due to severe noise, which could lead to inaccurate identification of time lags. When singularities appear in the cross-correlation due to noise,

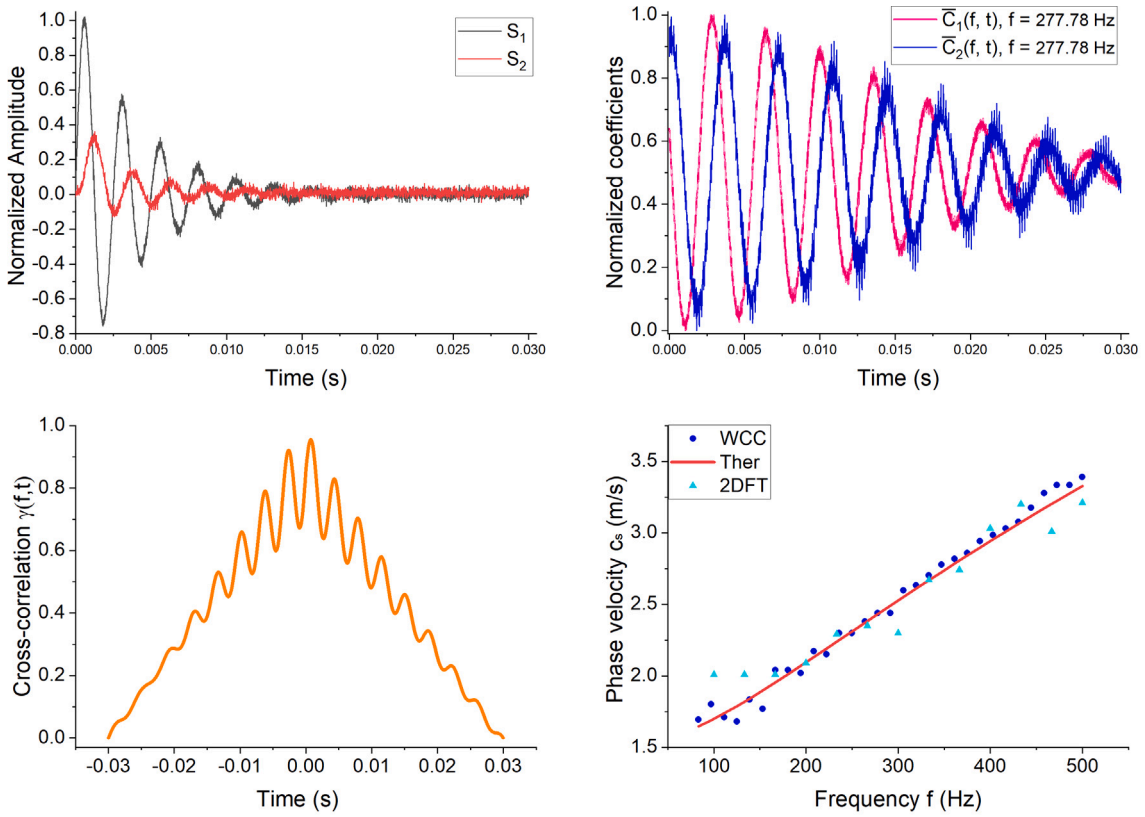

Fig. 6. The dispersion relation extracted from the noised signals with $SNR = 40$ dB. (a). The two noised signals S_1 and S_2; (b). The normalized CWT coefficients $\bar{C}_1(f,t)$ and $\bar{C}_2(f,t)$ of the noised signals at $f = 277.78$ Hz. (c). The cross-relation of the normalized CWT coefficients $\bar{C}_1(f,t)$ and $\bar{C}_2(f,t)$ in (b). (d). The dispersion relation extracted by the proposed method. **Ther**: Theoretical model.

Table 2
The AP of the dispersion extraction at different SNRs.

Noise levels	Case 1	Case 2
40 dB	0.97	0.95
20 dB	0.89	0.85
20 dB with filter	0.94	0.90

the designed 5-layer wavelet threshold filter is used to smooth the cross-correlation. Fig. 7(c) presents the noisy and filtered cross-correlation, where the point M_N is the maximum of the noised cross-correlation, caused by noise-induced singularities, leading to potential misinterpretation. With the designed filter, singularities in the filtered cross-correlation are smoothed, and the point M_F corresponds to the maximum of the cross-correlation, thus enhancing the stability of time lag identification. Fig. 7(d) shows the results of the proposed dispersion extraction method at an SNR of 20 dB, demonstrating greater stability and accuracy with the filter compared to the unfiltered results.

Table 2 summarizes the accuracy (AP) of the dispersion extraction results at SNRs of 40 dB and 20 dB (both with and without the filter) in 2 cases. It is observed that the proposed method achieves high accuracy in dispersion extraction across various noise levels. The dispersion extraction results based on 2DFT are also shown in Fig. 6(d) and Fig. 7(d) for different noise levels. For all cases (no noise, 40 dB noise, and 20 dB noise), the average accuracy (AP%) of the dispersion extraction results from 2DFT and WCC compared with the analytical solution are as follows: No noise: 97.3% (2DFT), 98.1% (WCC); 40 dB: 94.7% (2DFT), 96.0% (WCC); 20 dB: 83.2% (2DFT), 87.0% (WCC). From the comparison of these results, we observe that under lower noise conditions, the results of the two methods are quite similar. However, as the noise level increases, WCC demonstrates more stable results. This is because the noise significantly affects the frequency components of the signal at specific frequencies, and WCC, with its multi-scale nature, is able to analyze the signal at various resolutions, thereby reducing the impact of noise.

The signals with non-Gaussian random impulse noise were also analyzed and the results of the dispersion extraction using different methods are displayed in Fig. 8. From this figure, it is can be found that the FT-based method exhibits anomalies at 33.33 Hz. Furthermore, the performance of the WCC method is comparable to that of the FT method in the frequency range of 50 to 300 Hz. Beyond 300 Hz, the WCC method relatively outperforms the FT method. This is because the method based on WCC can

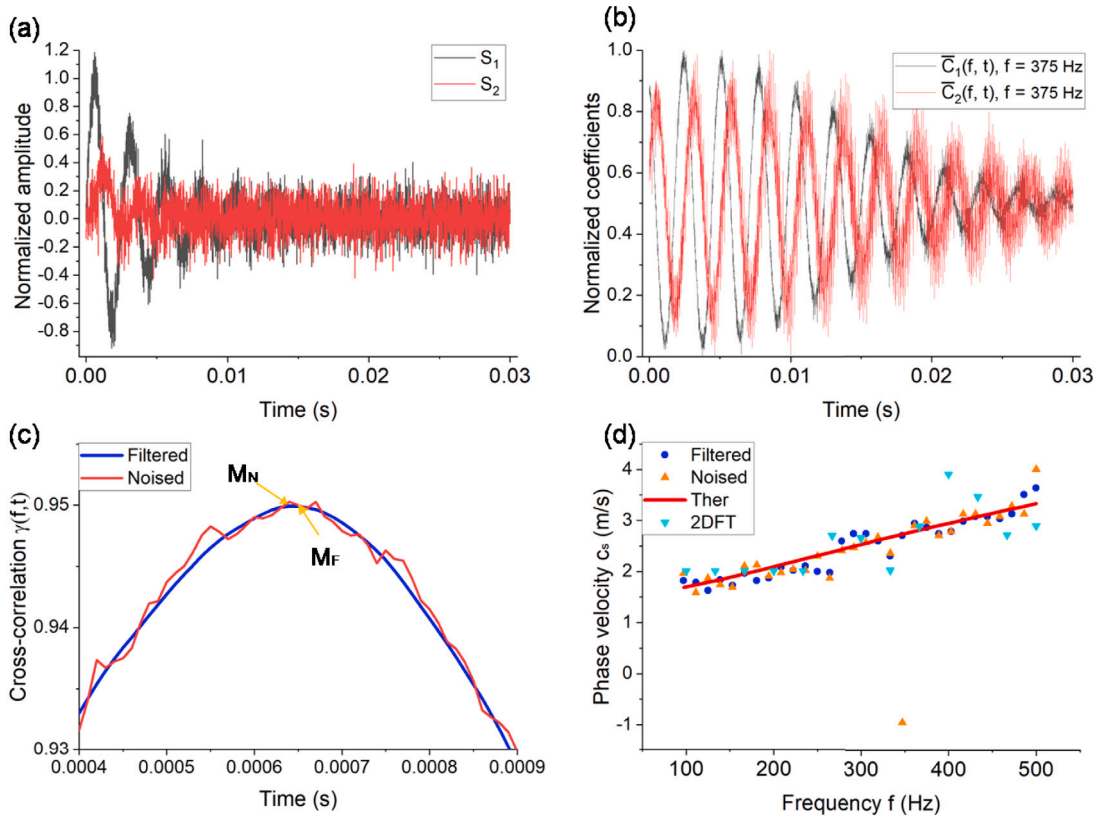

Fig. 7. The cross-correlation analysis of the noised signals with $SNR = 20$ dB. (a). The two noised signals S_1 and S_2; (b). The normalized CWT coefficients $\bar{C}_1(f,t)$ and $\bar{C}_2(f,t)$ of the noised signals at $f = 375$ Hz. (c). The cross-correlation of $\bar{C}_1(f,t)$ and $\bar{C}_2(f,t)$ when $\tau > 0.93$ and its corresponding filtered cross-correlation (d). The dispersion relation with and without the filter. **Ther**: Theoretical model.

Table 3
The accuracy of the SA-based inversion at each case.

Noise levels	AP(%): Mean±STD	
	μ_1	μ_2
No noises	99.5 ± 0.08	99.5 ± 0.6
40 dB	96.7 ± 3.9	98.5 ± 2.0
20 dB	94.7 ± 6.6	96.9 ± 4.2

provide local information of the signal in both time and frequency domains, with the capability of multi-resolution analysis. This allows the analysis of signals at different scales (resolutions). It can capture detailed features of impulse noise in high-frequency parts, while retaining the main components of the signal in low-frequency parts, thereby achieving effective noise suppression and signal preservation.

3.4. Inversion based on SA

Each parameter in the SA is allocated a substantial search range, with the shear modulus μ_1 and viscosity μ_2 for Cases 1 and 2 varying over ±50% of their true values. For Cases 1 and 2, the density is set to 1000 kg/m^3, which is a typical assumption for general soft tissues.

To test the accuracy of the inversion algorithm, dispersion relations based on noise-free signals (Fig. 4(b)), signals with an SNR of 40 dB (Fig. 6(d)), and signals with an SNR of 20 dB that have been filtered (Fig. 7(d)), are used for SA-based inversion testing. The accuracy of the inversion results for each case is displayed in Table 3, including the mean and the standard deviation(STD), for the 2 cases at different noise levels. It is observed that in each case, the inversion results demonstrate high accuracy. Therefore, the efficacy and accuracy of the proposed dispersion extraction method and inversion algorithm are verified. The calculations are performed on a computer with an Intel(R) Core(TM) i5-7200U CPU @ 2.50GHz processor. It can be found that the inversion takes approximately 3 s.

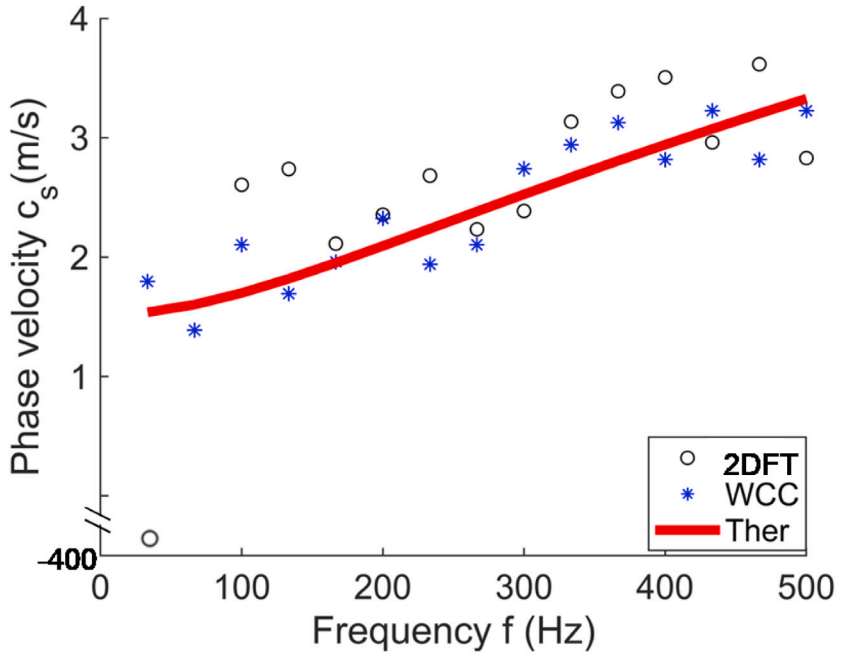

Fig. 8. Different methods for dispersion relation extraction. **Ther**: Theoretical model.

3.5. Discussions about the inversion

The sensitivity of the dispersion curve to the parameters μ_1 and μ_2 is related to the frequency range. The results of the sensitivity analysis for μ_1 and μ_2 using the theoretical dispersion relation from Case 2 are shown in Fig. 9. In this analysis, μ_1 (KPa) and μ_2 (Pa·s) are incremented by a proportional factor of 1.0–1.5 (with a step size of 0.01). For each disturbed parameter, the theoretical dispersion curve is computed and compared with the reference curve. The mean absolute error (MAE) is used as the sensitivity indicator, reflecting the overall deviation of the curve due to the parameter changes. Fig. 9(a) shows the sensitivity analysis from 1 to 100 Hz; we can see that the dispersion relation is significantly more sensitive to μ_1 in this frequency range. By analyzing the analytical dispersion relation, we find that when the frequency approaches 0, the phase velocity equals $\sqrt{\mu_1/\rho}$. However, for practical signals, the amplitude of the low-frequency components is relatively low, making it more susceptible to noise interference. This also requires higher demands on the data acquisition equipment, as low-frequency signals need longer sampling times to cover a complete cycle. Therefore, it is often difficult to extract accurate dispersion relations in the low-frequency range. Here, the dispersion relation in the 100 to 500 Hz range is used for analysis. Fig. 9(b) shows the sensitivity analysis in this range, where it can be observed that in this frequency range, the dispersion curve shows higher sensitivity to μ_2, providing a new opportunity for viscosity inversion. Therefore, we adopt a joint inversion method to characterize both μ_1 and μ_2. Fig. 10 shows the inversion process for different dispersion curves extracted from WCC in Case 1, with the contour plot of the objective function(loss) for different μ_1 and μ_2. From this plot, we can see that the objective function for this inversion process is a convex function. For convex functions, we can use the Grid Search (GS) method for inversion. The step sizes for μ_1 (KPa) and μ_2 (Pa s) are set to 10^{-3}, and the search range is ±50% of their true values. The inversion parameters are determined by finding the coordinates corresponding to the minimum value in the contour plot. The red points in the figure represent the GS inversion results. In Fig. 10(a), the inversion results using the dispersion in Fig. 5(a), and their comparison with SA show the following accuracies: μ_1 : 99.45% (SA), 95.04% (GS); μ_2 : 99.97% (SA), 99.96% (GS). The average computation times are: 3 s (SA), 22 s (GS). In Fig. 10(b), for the dispersion relation affected by stronger noise (Fig. 7(d)), the inversion results compared with SA show the following accuracies: μ_1 : 99.4% (SA), 85.2% (GS); μ_2 : 99.9% (SA), 97.1% (GS). Similarly, GS is also applied to the dispersion curve in Case 2 (Fig. 5(b)), with the following accuracies: μ_1 : 95.6% (SA), 93.6% (GS); μ_2 : 99.1% (SA), 98.7% (GS). The average computation times are: 3 s (SA), 300 s (GS).

From the comparison of these inversion results, we can observe that the SA-based method offers high accuracy and time efficiency in parameter inversion. GS is affected by the grid step size, where a smaller step size may lead to memory overload and excessive time cost. If the step size is too large, it may cause the optimal solution to be missed. In contrast, SA, through random walks in continuous space, can approach the exact optimal solution. GS itself is global (covering the entire parameter space), but due to discretization and computational cost, it may fail to "see" the true global optimum. On the other hand, SA can dynamically adjust the search range through random walks and cooling strategies, gradually approaching the optimal solution. We also observe the noise resistance of SA. This is because the dynamic search strategy of SA is more robust to noise interference (while GS is more sensitive to local fluctuations in the objective function). Noise causes significant fluctuations in the objective function at adjacent

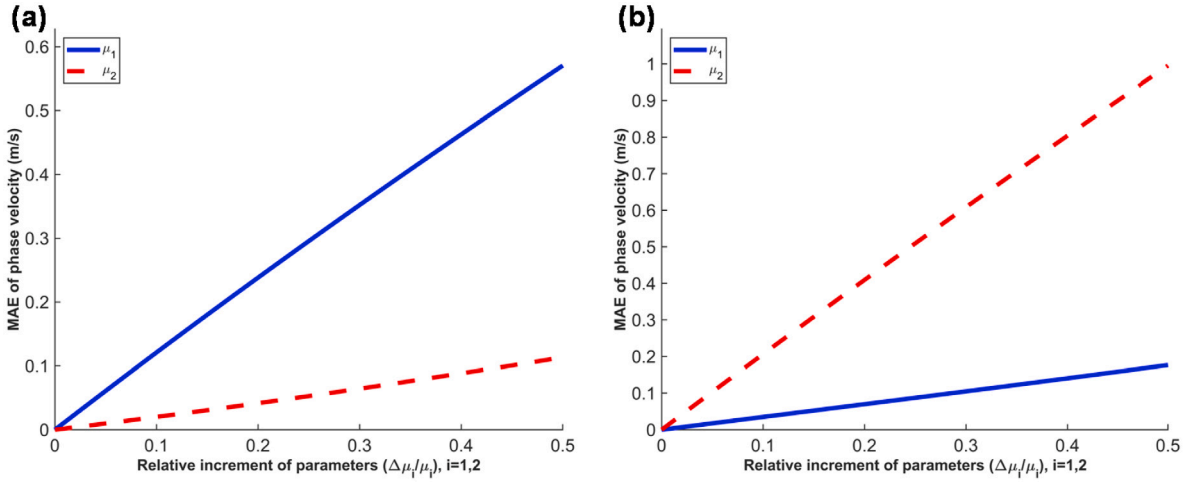

Fig. 9. The sensitivity analysis (a). 1 Hz to 100 Hz. (b). 100 to 500 Hz.

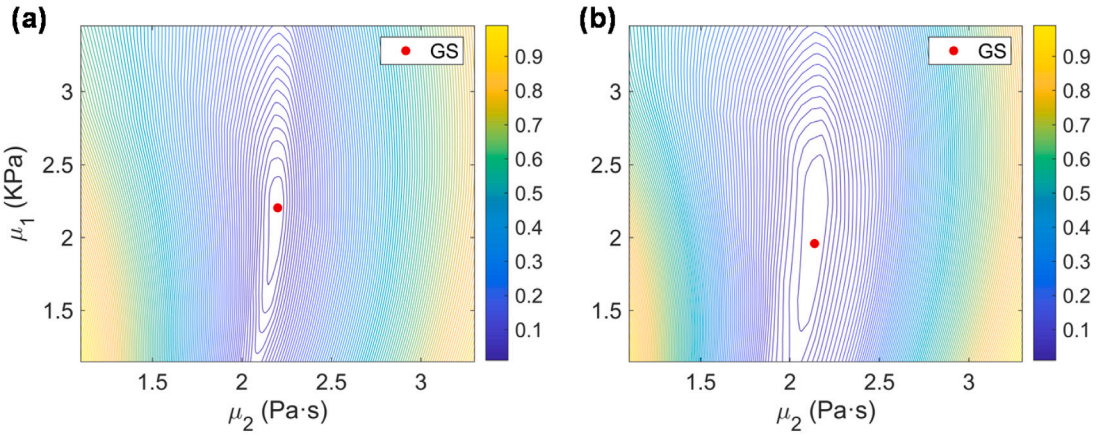

Fig. 10. Normalized contour plot and GS inversion for different dispersion relations. (a). Dispersion in Fig. 5(a). (b). Dispersion in Fig. 7(d).

grid points, which may lead GS to misjudge the optimal solution. The "rigid" selection of GS (only considering the minimum value at grid points) amplifies the noise impact, whereas the "flexible" search of SA (probabilistic acceptance) smooths the noise interference.

We also compared the inversion results with the least squares (LS) fitting method (as discussed in the work [36] using the three dispersion relations mentioned above. The LS method used in this study is based on the *trust region reflective* method in *MATLAB*. The inversion accuracy obtained are as follows: For Case 1 (No Noise): 92.1% (μ_1), 99.2% (μ_2). For Case 2 (No Noise): 94.8% (μ_1), 99.3% (μ_2). For Case 1 with 20 dB noise: 80.4% (μ_1), 96.7% (μ_2). From these results, we can observe that SA outperforms the LS method, particularly when stronger noise is present. This is because dispersion data is often influenced by noise and disturbances. LS is usually affected by these factors, leading to results that are overly dependent on local data characteristics, which may cause overfitting. In contrast, SA, due to its strong dynamic search ability, is better able to handle such noise or disturbances, finding more stable solutions. In terms of time efficiency, the average computation time for the LS method is 2 s, which is more efficient compared to SA. However, since the forward process in this study has an analytical solution, the efficiency of SA is acceptable. Considering both accuracy and time efficiency, SA is a highly recommended method for the problem addressed in this study.

4. Experimental application

This study utilized shear ultrasonic wave experimental data to validate the proposed method. The ultrasonic waveform data used were provided by Bhatt et al. (2021) [46]. This work implemented a SWE sequence to assess the biomechanical properties of farm-raised fatty duck livers (foie gras). This research involved nine mulard ducks used for the production of foie gras. The experiment received approval from the Institutional Animal Care and Ethics Committee at the University of Montréal Hospital Research Centre. During a two-week pre-feeding period, the ducks had free access to feed. After this pre-feeding period, the ducks underwent 12 days of force-feeding twice daily via a mechanical tube with humidified corn kernels (40% water and 60% dry corn kernels). The

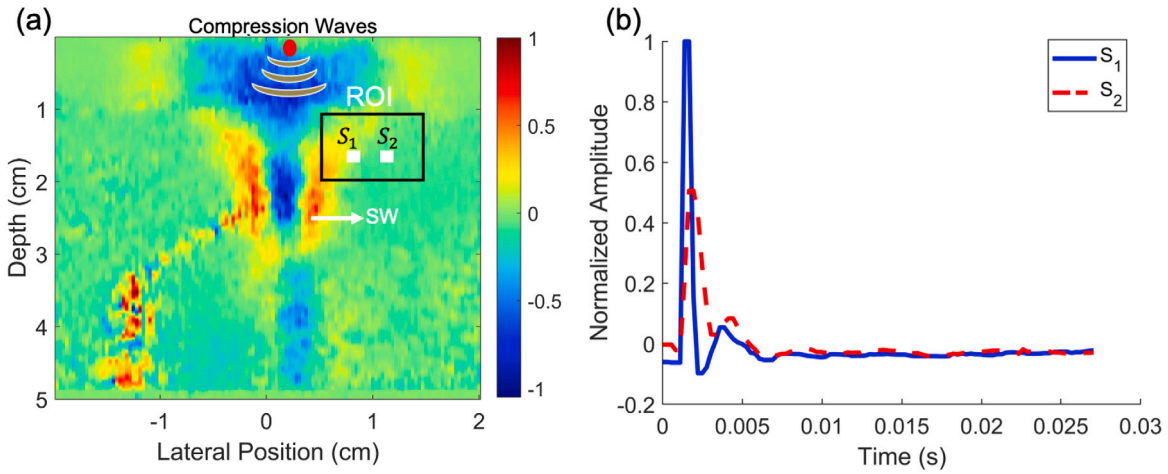

Fig. 11. The shear wave acquisition in the specimen. (a). The position of measurement. (b). An example of a signal pair of the recorded shear wave waveforms: S_1 and S_2.

amount of food gradually increased from about 350 grams at the beginning of the feeding period to 650 grams per meal. Ultrasound measurements were taken on the farm on the 1st, 5th, 9th, and 12th days of the force-feeding period. During measurements, the ducks remained awake (no anesthesia) and were manually restrained in a dorsal position by a veterinarian. Ultrasound measurements were conducted using a Verasonics Vantage programmable system and an ATL L7-4 linear probe (the specifications: number of elements 128; center frequency 5 MHz; element pitch 0.298 mm; element length 7 mm; number of transmitting elements 64; number of receiving elements 128). The probe was placed on the duck liver for real-time B-mode imaging, and the focus point was manually selected within a depth of 1 cm. In shear wave elastography mode, five focused acoustic radiation pushes were applied using 64 elements of the probe. Each push lasted 198.4 ms and was positioned from −5 to 5 mm in depth from the focal zone with steps of 2.5 mm. When measuring shear wave propagation, 5 pushes in depth are performed to generate shear waves. The SWE sequence was repeated 5 times for data averaging. This means there were 5 instances of shear wave propagation, each following one after another with a given latent period. A single acquisition included 100 radio frequency frames for shear wave tracking. Beamforming was performed using the f-k migration method, which enhances beamforming accuracy and image reconstruction by transforming the signal into the frequency and wavenumber domains, achieving a frame rate of 3623 Hz for shear wave displacement tracking [47]. The liver profiles of the investigated ducks were manually delineated based on the veterinarian's experience. More experimental details can be found in the work [46].

Fig. 11(a) shows the propagation of the shear wave in an ultrasound image of the duck liver at a certain frame, where the acoustic radiation force excitation of the shear wave can be seen. To capture the required two-point shear wave signals (S_1 and S_2), a 1 cm × 1 cm region of interest (ROI) on the liver is marked for signal extraction. The selection of the ROI involves choosing a region where the shear wave front can be clearly observed as it propagates. Fig. 11(a) provides a example of positions for S_1 and S_2, with a spacing of 3.125 mm. Since S_1 and S_2 move across different rows and columns within the ROI, most points within the ROI are accessed. Fig. 11(b) shows an example of a raw waveform signal pair. These figures are produced using waveform data provided by the work [46]. Given the constraints of the limited number of radio frequency frames collected, time-domain interpolation techniques were applied to the raw waveform data to enhance its continuity and smoothness.

For a pair of signals, the WCC-based method can be used for dispersion relation extraction. As mentioned in Section 3.2, it is possible to set different frequency intervals to obtain more phase velocities, and then merge these phase velocities to perform outlier removal. To reduce noise interference and improve the stability of the dispersion relation extraction, within the ROI, the signal pair can be moved in a fixed interval along the row and column directions to obtain the dispersion curve extraction results from multiple signal pairs. These dispersion relations can be processed for outlier removal and averaging, and smoothing filter treatment, to obtain a smooth and continuous dispersion relation for the detected duck liver ultrasound shear wave. Fig. 12 displays the dispersion relations extracted using the WCC method from one example measurement taken on the 1st, 5th, 9th, and 12th days across the frequency range of 75 Hz to 300 Hz. The dispersion relation extracted by the 2DFT method is also plotted. Based on the dispersion relations corresponding to the viscoelastic properties inverted using the SA algorithm and the experimental dispersion data, it can be found that the algorithm's outputs fit the experimental results well.

The work utilizes five shear wave data at each time point (Day 1, 5, 9, and 12) to extract dispersion curves, respectively. Subsequently, the viscoelastic properties μ_1 and μ_2 are inverted using each dispersion curve. The mean and STD of the inverted results for viscoelastic properties at each time point are displayed in Fig. 13. The value change of $\mu_1(KPa)$ and $\mu_2(Pa * s)$ at different time points (Day 1, Day 5, Day 9, and Day 12) can be found as follows. During the four time points measured, μ_1 generally showed an upward trend. The greatest rate of increase occurred from Day 5 to Day 9, with μ_1 rising by 35.8% compared to Day 5, with the rate of increase slowing from Day 9 to Day 12. μ_2 also displayed an overall upward trend during this period. The increase

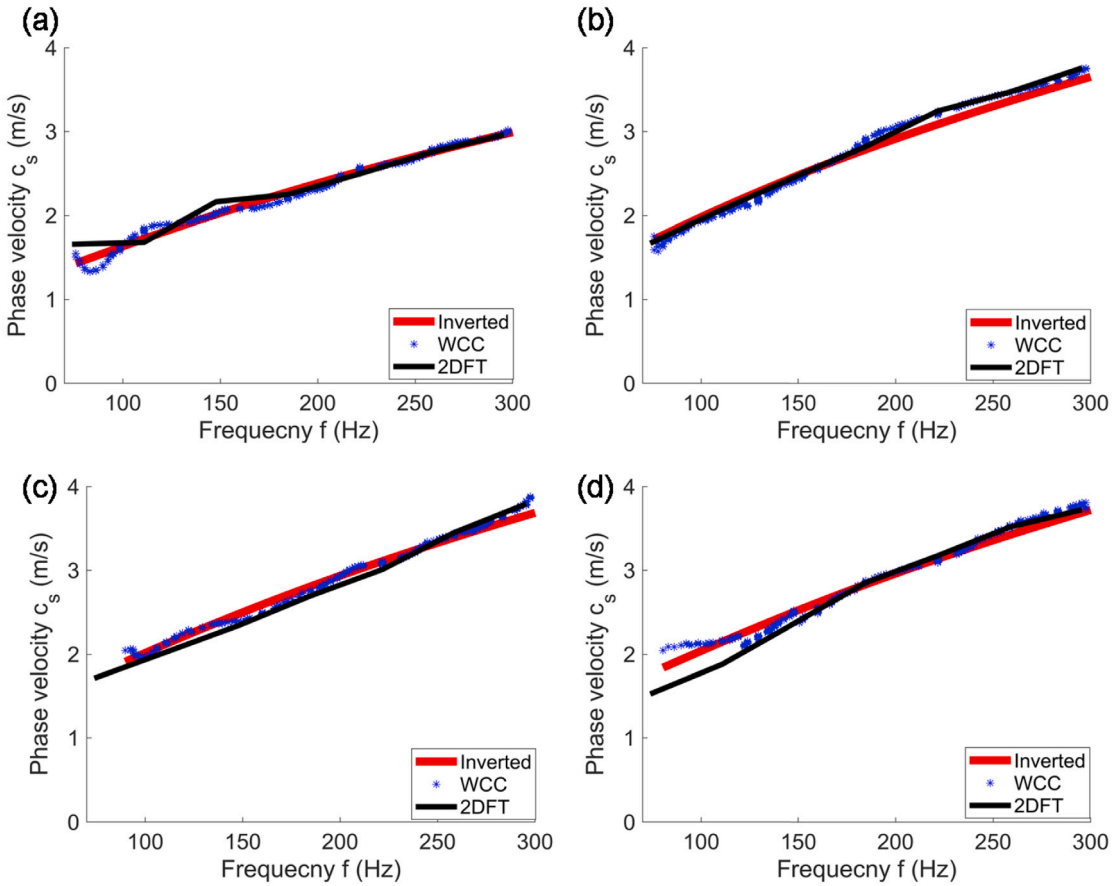

Fig. 12. The experimental and inverted dispersion relation curves of the ultrasound shear waves. **Inverted**: inverted dispersion relation curves. **WCC**: WCC-extracted experimental dispersion relation curves. **2DFT**: dispersion relation using 2DFT. (a). Day 1. (b) Day 5. (c). Day 9. (d). Day 12.

was most significant in the first four days, with μ_2 rising by 45.38% from Day 1 to Day 5. The growth rate of μ_2 slowed after Day 5. These data not only provide a scientific basis for the optimization of duck liver quality but also offer references for the formulation of further feeding and management strategies.

5. Discussions and conclusion

This paper proposes a method for the inversion of viscoelastic properties of soft tissues based on ultrasound shear wave dispersion. This method initially uses the WCC method to extract dispersion relations from shear wave signals, followed by the use of the SA algorithm and the forward model to achieve the inversion of viscoelastic properties. The feasibility and accuracy of the proposed method are validated through numerical analysis and experimental animals in vivo.

In the numerical analysis, the performance of the proposed method was analyzed across different soft tissues and under various noise conditions. Subsequently, the raw data provided by the study [46] were used for experimental validation. In the work [46], viscoelasticity was assessed at two specific frequencies: 75 Hz and 202 Hz, combining attenuation and dispersion information. In contrast, this study uses the dispersion relation within the frequency range of 100 Hz to 300 Hz for viscoelastic characterization, which may lead to different results. Additionally, variations in signal processing methods, such as filtering techniques, can contribute to differences in the viscoelastic characterization results. Despite these variations, the general trend in the viscoelasticity of duck liver with feeding days remains consistent across different characterization methods.

This method has several advantages: 1. The method based on WCC employs multi-scale analysis, which has the potential to accurately acquire phase velocity data across various frequency ranges. 2. The inversion method proposed can estimate shear modulus and viscosity solely based on the dispersion curve and the viscoelastic model. This convenience can enhance the efficiency of characterizing soft tissues. 3. The method uses the dispersion relation curve within an interval for the inversion of viscoelastic properties. Compared to the method in the study [46] that just estimated the viscoelasticity at specific frequency points employing attenuation coefficients and phase velocity, this paper's approach provides efficiency.

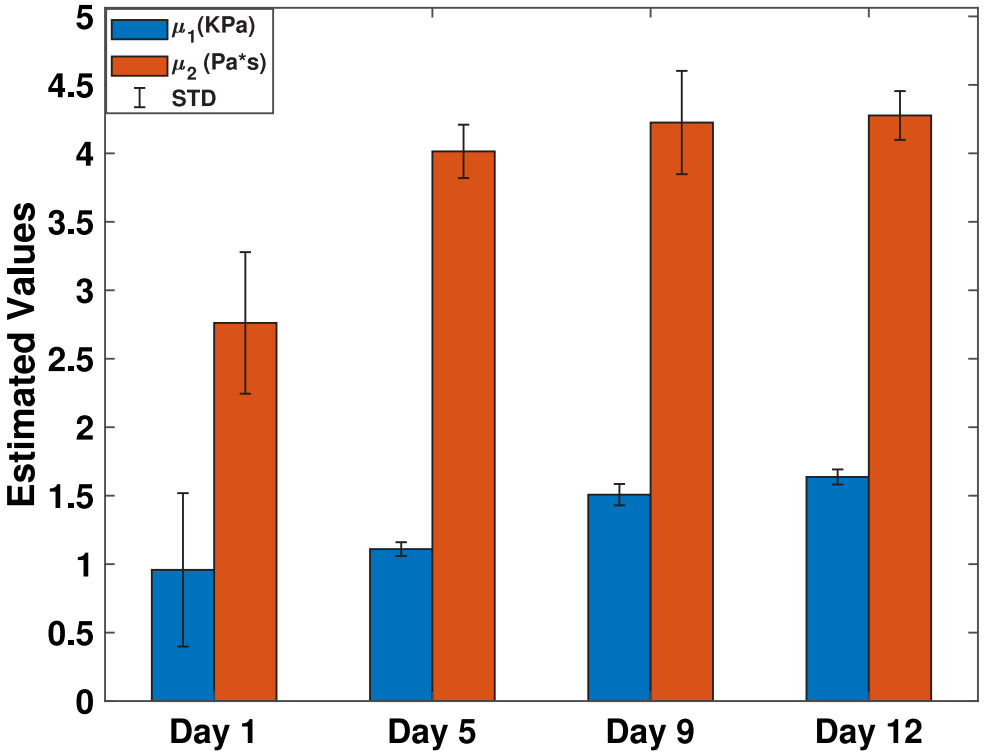

Fig. 13. The inversion results of viscoelasticity.

However, some issues also need attention: 1. During the process of measuring shear waves, the influence of noise might affect the results of dispersion extraction. Moreover, other kinds of waves, such as longitudinal waves and guided waves, may also impact the measurement results. To improve the stability of dispersion extraction, this paper uses a multi-point measurement method within the ROI. 2. To enhance the accuracy of the estimated results, future studies could also combine the phase velocity dispersion curves with attenuation coefficients across frequency bands to jointly invert for viscoelasticity. 3. In this study, a rheological model (Kelvin–Voigt model), is employed to assess viscosity. It is essential to recognize that the parameters of this model may be influenced by the development of certain pathologies, which could introduce biases in diagnosis. For example, the rheological behavior of the liver may change in response to variations in its fat content. 4. In practical applications, initiating the inversion process can be challenging if the dispersion information are not well understood. Fortunately, previous studies [48,49], have provided the viscoelastic properties of different soft tissues. These prior research findings can serve as prior information for initialization and determining the search range, thus providing valuable references for the inversion process. In this paper, SA is employed as the tool for inversion. The choice of SA is due to its global optimality and efficiency. Although this study focused on two parameters under the assumption of a single-layer soft tissue, future research will assume multilayer soft tissues. In such cases, where parameters across different layers need to be inverted, local optimization issues can become more severe, further showcasing the advantages of the SA model used in this study.

In this study, the ARF is employed to generate shear waves. This method is sensitive to the incident angle of the probe. Variations in the incident angle may affect the excitation efficiency, propagation path of shear waves, and subsequent elastic parameter measurements, potentially reducing the accuracy and repeatability of the results [50]. To address this issue, this study adopted a perpendicular incidence approach between the probe and the soft tissue surface. The main advantages of this approach are as follows: the method can ensure that the shear wave excitation direction aligns with the propagation direction of the sound waves. This enhances the excitation efficiency of shear waves. Perpendicular incidence avoids deviations in the shear wave propagation direction, improving wave purity and predictability. Perpendicular incidence reduces multipath propagation and signal interference, enhancing the intensity and SNR of shear waves. Therefore, maintaining the perpendicular incident angle between the probe and the tissue surface during practical operations is critical for achieving high-precision and high-reliability soft tissue elasticity assessments. For excitation methods involving non-perpendicular incident angles, future research could focus on developing corresponding analytical models to enable accurate viscoelastic property analysis under various incident angles.

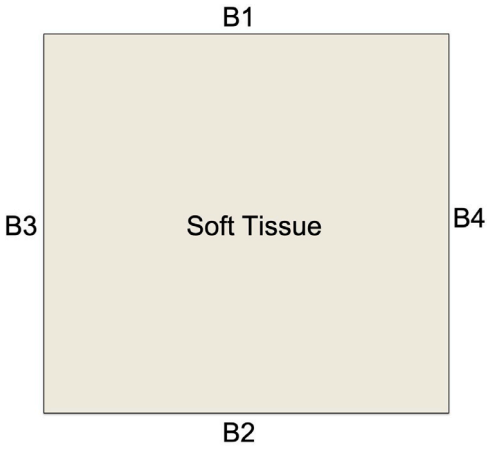

Fig. A.14. The schematic of the FEM model.

CRediT authorship contribution statement

Shihao Cui: Writing – original draft, Visualization, Validation, Software, Methodology, Investigation, Formal analysis, Data curation, Conceptualization. **Guy Cloutier:** Writing – review & editing, Resources, Investigation, Formal analysis, Data curation. **Marie-Hélène Roy Cardinal:** Writing – review & editing, Data curation. **Houman Savoji:** Writing – review & editing, Supervision, Resources, Project administration, Methodology, Investigation, Funding acquisition, Formal analysis, Conceptualization. **Pooneh Maghoul:** Writing – review & editing, Supervision, Resources, Project administration, Methodology, Investigation, Funding acquisition, Formal analysis, Conceptualization.

Declaration of competing interest

The authors declare that they have no known competing financial interests or personal relationships that could have appeared to influence the work reported in this paper.

Acknowledgments

The authors acknowledge the financial support of the Fonds de recherche du Québec (FRQ) AUDACE program.

Appendix A. Numerical simulation

In the FEM model by the software *COMSOL*, a 2D simulation area is depicted in Fig. A.14, which is a square with each side measuring 0.2 m. The boundary $B1$ is set as a free boundary condition, while the other boundaries $B2$, $B3$, and $B4$ are assigned low-reflection boundary conditions. More details on the viscoelastic simulation of soft tissues can be found in the literature [51].

Appendix B. Wavelet threshold filter

To mitigate the singularities introduced by noise in cross-correlation, which could hinder the accurate identification of time lags, a filter utilizing discrete wavelet transform (DWT) is implemented. DWT evolves from the discretization of CWT. Mallat's efficient method for DWT enables it to function as a filter, separating the signal into low-frequency (approximation coefficients, cA) and high-frequency (detail coefficients, cD) components [52]. In this context, cA captures the signal's overall trend, while cD encapsulates detailed aspects.

In this research, a 5-level DWT-based filter is developed for filtering in cross-correlation analysis. The initial level of DWT decomposes the input signal into cA and cD. Subsequent levels, from the second to the fifth, employ heuristic soft thresholding on the cD from the prior level's decomposition. The thresholded outcomes are then inversely transformed using inverse DWT at each stage, yielding the reconstructed filtered signal.

Data availability

Data will be made available on request.

References

[1] A. Fausto, D. Rubello, A. Carboni, P. Mastellari, S. Chondrogiannis, L. Volterrani, Clinical value of relative quantification ultrasound elastography in characterizing breast tumors, Biomed. Pharmacother. 75 (2015) 88–92.

[2] G. Cismaru, T. Serban, A. Tirpe, Ultrasound methods in the evaluation of atherosclerosis: From pathophysiology to clinic, Biomedicines 9 (4) (2021) 418.

[3] V. Kanagaraju, P. Ashlyin, N. Elango, B. Devanand, Role of transrectal ultrasound elastography in the diagnosis of prostate carcinoma, J. Med. Ultrasound 28 (3) (2020) 173–178.

[4] R. Li, J. Guo, Y. Duan, X. Liu, L. Gui, Y. Xu, X. Kong, Y. Li, H. Chen, Z. Yuan, Monitoring inflammation-cancer progression by cell viscosity, polarity and leucine aminopeptidase using multicolor fluorescent probe, Chem. Eng. J. 435 (2022) 135043.

[5] Y. Abidine, A. Giannetti, J. Revilloud, V.M. Laurent, C. Verdier, Viscoelastic properties in cancer: From cells to spheroids, Cells 10 (7) (2021) 1704.

[6] Y. Zhu, Y. Zheng, Y.-y. Shen, X. Chen, X.-y. Zhang, H.-m. Lin, Y.-r. Guo, T.-f. Wang, S.-p. Chen, Analyzing and modeling rheological behavior of liver fibrosis in rats using shear viscoelastic moduli, J. Zhejiang Univ. Sci. B 15 (4) (2014) 375.

[7] Y.-H. Jeong, B. Kevin, J.-H. Ahn, R. Chaudhary, M.G. Kang, H.W. Park, J.-S. Koh, Y. Park, U.S. Tantry, P.A. Gurbel, Viscoelastic properties of clot formation and their clinical impact in East Asian versus caucasian patients with stable coronary artery disease: a COMPARE-RACE analysis, J. Thromb. Thrombolysis 51 (2021) 454–465.

[8] A. Stocchi, C. Bernal, A. Vázquez, J. Biagotti, J. Kenny, A silicone treatment compared to traditional natural fiber treatments: effect on the mechanical and viscoelastic properties of jute—vinylester laminates, J. Compos. Mater. 41 (16) (2007) 2005–2024.

[9] J. Ibrulj, E. Dzaferovic, M. Obucina, M.K. Kuzman, Numerical and experimental investigations of polymer viscoelastic materials obtained by 3D printing, Polymers 13 (19) (2021) 3276.

[10] K. Kim, W.R. Wagner, Non-invasive and non-destructive characterization of tissue engineered constructs using ultrasound imaging technologies: a review, Ann. Biomed. Eng. 44 (2016) 621–635.

[11] N. Arnold, J. Scott, T.R. Bush, A review of the characterizations of soft tissues used in human body modeling: scope, limitations, and the path forward, J. Tissue Viability 32 (2) (2023) 286–304.

[12] S. Qiu, X. Zhao, J. Chen, J. Zeng, S. Chen, L. Chen, Y. Meng, B. Liu, H. Shan, M. Gao, et al., Characterizing viscoelastic properties of breast cancer tissue in a mouse model using indentation, J. Biomech. 69 (2018) 81–89.

[13] A. Genovese, S.R. Pastore, Development of a portable instrument for non-destructive characterization of the polymers viscoelastic properties, Mech. Syst. Signal Process. 150 (2021) 107259.

[14] A. Manduca, P.V. Bayly, R.L. Ehman, A. Kolipaka, T.J. Royston, I. Sack, R. Sinkus, B.E. Van Beers, MR elastography: Principles, guidelines, and terminology, Magn. Reson. Med. 85 (5) (2021) 2377–2390.

[15] N. Salameh, F. Peeters, R. Sinkus, J. Abarca-Quinones, L. Annet, L.C. Ter Beek, I. Leclercq, B.E. Van Beers, Hepatic viscoelastic parameters measured with MR elastography: correlations with quantitative analysis of liver fibrosis in the rat, J. Magn. Reson. Imaging: Off. J. Int. Soc. Magn. Reson. Med. 26 (4) (2007) 956–962.

[16] I. Sack, J. Rump, T. Elgeti, A. Samani, J. Braun, MR elastography of the human heart: noninvasive assessment of myocardial elasticity changes by shear wave amplitude variations, Magn. Reson. Med.: Off. J. Int. Soc. Magn. Reson. Med. 61 (3) (2009) 668–677.

[17] J. Brum, G. Balay, D. Bia, N. Benech, A. Ramos, R. Armentano, C. Negreira, Improvement of Young modulus estimation by ultrasound using static pressure steps, Phys. Procedia 3 (1) (2010) 1087–1094.

[18] M. Ashikuzzaman, A. Héroux, A. Tang, G. Cloutier, H. Rivaz, Displacement tracking techniques in ultrasound elastography: From cross-correlation to deep learning, IEEE Trans. Ultrason. Ferroelectr. Freq. Control (2024).

[19] L. Castera, X. Forns, A. Alberti, Non-invasive evaluation of liver fibrosis using transient elastography, J. Hepatol. 48 (5) (2008) 835–847.

[20] H. Li, G. Flé, M. Bhatt, Z. Qu, S. Ghazavi, L. Yazdani, G. Bosio, I. Rafati, G. Cloutier, Viscoelasticity imaging of biological tissues and single cells using shear wave propagation, Front. Phys. 9 (2021) 666192.

[21] P. Song, S. Chen, Shear wave dispersion ultrasound vibrometry, in: Ultrasound Elastography for Biomedical Applications and Medicine, Wiley Online Library, 2018, pp. 284–294.

[22] L. Yazdani, I. Rafati, M. Gesnik, F. Nicolet, B. Chayer, G. Gilbert, A. Volniansky, D. Olivié, J.-M. Giard, G. Sebastiani, et al., Ultrasound shear wave attenuation imaging for grading liver steatosis in volunteers and patients with non-alcoholic fatty liver disease: A pilot study, Ultrasound Med. Biol. 49 (10) (2023) 2264–2272.

[23] X.-q. Zhang, R.-q. Zheng, J.-y. Jin, J.-f. Wang, T. Zhang, J. Zeng, US shear-wave elastography dispersion for characterization of chronic liver disease, Radiology 305 (3) (2022) 597–605.

[24] J. Ormachea, K.J. Parker, R.G. Barr, An initial study of complete 2D shear wave dispersion images using a reverberant shear wave field, Phys. Med. Biol. 64 (14) (2019) 145009.

[25] N. Nitta, M. Yamakawa, H. Hachiya, T. Shiina, A review of physical and engineering factors potentially affecting shear wave elastography, J. Med. Ultrason. 48 (4) (2021) 403–414.

[26] T. Deffieux, G. Montaldo, M. Tanter, M. Fink, Shear wave spectroscopy for in vivo quantification of human soft tissues visco-elasticity, IEEE Trans. Med. Imaging 28 (3) (2008) 313–322.

[27] M. Muller, J.-L. Gennisson, T. Deffieux, M. Tanter, M. Fink, Quantitative viscoelasticity mapping of human liver using supersonic shear imaging: preliminary in vivo feasibility study, Ultrasound Med. Biol. 35 (2) (2009) 219–229.

[28] C.T. Barry, B. Mills, Z. Hah, R.A. Mooney, C.K. Ryan, D.J. Rubens, K.J. Parker, Shear wave dispersion measures liver steatosis, Ultrasound Med. Biol. 38 (2) (2012) 175–182.

[29] P. Kijanka, M.W. Urban, Dispersion curve calculation in viscoelastic tissue-mimicking materials using non-parametric, parametric, and high-resolution methods, Ultrasonics 109 (2021) 106257.

[30] P. Kijanka, B. Qiang, P. Song, C.A. Carrascal, S. Chen, M.W. Urban, Robust phase velocity dispersion estimation of viscoelastic materials used for medical applications based on the multiple signal classification method, IEEE Trans. Ultrason. Ferroelectr. Freq. Control 65 (3) (2018) 423–439.

[31] P. Kijanka, L. Ambrozinski, M.W. Urban, Two point method for robust shear wave phase velocity dispersion estimation of viscoelastic materials, Ultrasound Med. Biol. 45 (9) (2019) 2540–2553.

[32] Q. Wu, X. Zheng, J. Pan, F. Zhang, G. Zhang, Measurement of interstation phase velocity by wavelet transformation, Earthq. Sci. 22 (2009) 425–429.

[33] X. Yang, Chapter 6 - genetic algorithms, in: X.-S. Yang (Ed.), Nature-Inspired Optimization Algorithms (Second Edition), second ed., Academic Press, 2021, pp. 91–100.

[34] J. Mura, F. Schrank, I. Sack, An analytical solution to the dispersion-by-inversion problem in magnetic resonance elastography, Magn. Reson. Med. 84 (1) (2020) 61–71.

[35] C.F. Otesteanu, B.R. Chintada, M.B. Rominger, S.J. Sanabria, O. Goksel, Spectral quantification of nonlinear elasticity using acoustoelasticity and shear-wave dispersion, IEEE Trans. Ultrason. Ferroelectr. Freq. Control 66 (12) (2019) 1845–1855.

[36] B. Cai, T. Li, L. Bo, J. Li, R. Sullivan, C. Sun, W. Huberty, Z. Tian, Development of a piezo stack–laser doppler vibrometer sensing approach for characterizing shear wave dispersion and local viscoelastic property distributions, Mech. Syst. Signal Process. 214 (2024) 111389.

[37] S. Catheline, J.-L. Gennisson, G. Delon, M. Fink, R. Sinkus, S. Abouelkaram, J. Culioli, Measurement of viscoelastic properties of homogeneous soft solid using transient elastography: An inverse problem approach, J. Acoust. Soc. Am. 116 (6) (2004) 3734–3741.
[38] S. Chen, M. Fatemi, J.F. Greenleaf, Quantifying elasticity and viscosity from measurement of shear wave speed dispersion, J. Acoust. Soc. Am. 115 (6) (2004) 2781–2785.
[39] S. Cui, P. Maghoul, X. Liang, N. Wu, Q. Wang, Structural fatigue crack localisation based on spatially distributed entropy and wavelet transform, Eng. Struct. 266 (2022) 114544.
[40] V.K. Sudarshan, U.R. Acharya, S.L. Oh, M. Adam, J.H. Tan, C.K. Chua, K.P. Chua, R. San Tan, Automated diagnosis of congestive heart failure using dual tree complex wavelet transform and statistical features extracted from 2 s of ECG signals, Comput. Biol. Med. 83 (2017) 48–58.
[41] Z. Chik, T. Islam, M. Mustafa, H. Sanusi, S. Rosyidi, M. Taha, Surface wave analysis using Morlet wavelet in geotechnical investigations, J. Appl. Sci. 9 (19) (2009) 3491–3501.
[42] Y. Ma, C. Peng, W. Gui, F.-y. Wang, Transient mould friction based on the wavelet theory, J. Iron Steel Res. Int. 22 (9) (2015) 785–794.
[43] Z. Cheng, J. Pellettiere, Correlation analysis of automobile crash responses based on wavelet decompositions, Mech. Syst. Signal Process. 17 (6) (2003) 1237–1257.
[44] W. Liao, D. Li, S. Cui, A heuristic optimization algorithm for HMM based on SA and EM in machinery diagnosis, J. Intell. Manuf. 29 (2018) 1845–1857.
[45] C. Amador, M.W. Urban, L.V. Warner, J.F. Greenleaf, In vitro renal cortex elasticity and viscosity measurements with shearwave dispersion ultrasound vibrometry (SDUV) on swine kidney, in: 2009 Annual International Conference of the IEEE Engineering in Medicine and Biology Society, IEEE, 2009, pp. 4428–4431.
[46] M. Bhatt, L. Yazdani, F. Destrempes, L. Allard, B.N. Nguyen, A. Tang, G. Cloutier, Multiparametric in vivo ultrasound shear wave viscoelastography on farm-raised fatty duck livers: human radiology imaging applied to food sciences, Poult. Sci. 100 (4) (2021) 100968.
[47] D. Garcia, L. Le Tarnec, S. Muth, E. Montagnon, J. Porée, G. Cloutier, Stolt's fk migration for plane wave ultrasound imaging, IEEE Trans. Ultrason. Ferroelectr. Freq. Control 60 (9) (2013) 1853–1867.
[48] M. W. Urban, S. Chen, M. Fatemi, A review of shearwave dispersion ultrasound vibrometry (SDUV) and its applications, Curr. Med. Imaging 8 (1) (2012) 27–36.
[49] G. Singh, A. Chanda, Mechanical properties of whole-body soft human tissues: a review, Biomed. Mater. 16 (6) (2021) 062004.
[50] W.T. Lim, E.H. Ooi, J.J. Foo, K.H. Ng, J.H. Wong, S.S. Leong, Shear wave elastography: a review on the confounding factors and their potential mitigation in detecting chronic kidney disease, Ultrasound Med. Biol. 47 (8) (2021) 2033–2047.
[51] H. Lin, S. Chen, T. Wang, Simulation study on viscoelasticity measurement of soft tissue using the surface wave method, J. Shenzhen Univ. Sci. Eng. (Chinese) 30 (3) (2013) 261–267.
[52] S.G. Mallat, Multiresolution approximations and wavelet orthonormal bases of $L^2(R)$, Trans. Amer. Math. Soc. 315 (1) (1989) 69–87.